PROLATE ELLIPSOIDAL LENS FOR ANTENNA SYSTEMS PROVIDING MULTIPLE ASYMMETRIC BEAMS

Marco Letizia[*]**, Jean F. Zürcher, and Juan R. Mosig**

Laboratory of Electromagnetics and Acoustics (LEMA), Ecole Polytechnique Fédérale de Lausanne (EPFL), EPFL Station 11, Lausanne CH-1015, Switzerland

Abstract—A 3-D shaped prolate ellipsoidal dielectric lens is designed to produce multiple asymmetric beams in Ka-band. Such radiation characteristics are useful in applications where the antenna system is mounted on platforms flying above Earth and the shape of the footprints have to be carefully controlled for different elevation angles. A set of design rules is introduced and the final designs are optimized using full-wave time-domain methods. A fully operational Ka-band antenna subsystem has been prototyped and measured. The final antenna lens has axes lengths of 62.3 mm and 57.8 mm and provides a maximum gain of 21 dB. When mounted on a stabilized platform at the altitude of 21 km (a typical HAPS scenario), this antenna provides 19 circular ground footprints of 5 km diameter each. Radiation pattern measurements show that such a lens reduces the natural beam footprint elongation unavoidable with traditional spherical lenses and confirm the validity of the proposed system.

1. INTRODUCTION

Many systems for communications, navigation, and surveillance, require the use of high gain multi-beam antennas. Typical examples are ground base-station terminals [1], radar systems [2], geostationary satellites [3], LEO-satellites [4] and High Altitude Platform Stations (HAPS) [5]. Multiple beams allow increasing the capacity of the communication channel by implementing beam-switching and a multi-cell frequency reuse scheme between different beams [6].

Nowadays, the mm-wave band is considered as very promising for these applications, due to the relative small size of the antennas

* Corresponding author: Marco Letizia (marco.letizia@epfl.ch).

and to the larger bandwidth available at these frequencies. Antenna systems based on lenses and reflectors are considered the most compact and efficient solutions for multi-beam applications in this band [7, 8]. Especially, lens solutions are becoming particularly interesting. Compared with reflectors, lenses are lighter and more tolerant to surface manufacturing errors. They also allow much more flexible designs ranging from very high gain antenna pencil beams tailor-made beams with special footprint shapes. Finally, lenses suffer much less from the inherent blockage due to the primary feeds [9].

Controlling the beam patterns of a multi-beam antenna system is often a key issue of the design. For instance, the link budget and the geographic coverage of a system are both strongly influenced by the gain, the aperture, and the shape of the beams [10–12]. If used on an aerial station, circular and symmetric multi-beams would produce a circular footprint in the cell just below the antenna but elliptical footprints in all the remaining cells. The elongation of such footprints increases with the elevation/polar angle θ, degrading the performance of the communication system [13–15]. However, circular footprints are highly desirable in such systems, providing better geographic coverage and more uniform link budgets across the coverage area [9]. For an aerial station to generate equal and circular footprints, asymmetric antenna beams are the obvious solution.

Synthesis and characterization of asymmetric beams have been addressed in previous publications [16–18]. These contributions were primarily focused on printed antenna arrays, which are not well suited for Ka-band, since it is well known [19–21] that the total efficiency of printed arrays including the associated printed feeding networks quickly deteriorates at mm-wave frequencies. Lens antennas are considered as an attractive alternative to generate shaped beams at mm-waves, as witnessed by many recently published papers proposing optimized lens shapes to produce various kinds of patterns. See for instance [22, 23].

To the best of our knowledge, optimized spherical dielectric lenses were considered in the past to generate single shaped-beams but they have never been studied to produce multiple beams, able to guarantee equal and circular ground footprints for communications from aerial stations. Such lenses would also be very interesting and efficient for applications where the antenna beams need to be shaped in the two radiating planes.

In typical LEO-satellites and HAPS scenarios, circular polarization is a required feature. This does not interfere with the proposed design, as circular polarization is easily achieved either by using circularly polarized primary sources or with the help of external polarizers [24].

In this paper, we propose a multi-beam lens antenna design in which the beam symmetry is controlled by acting on the lens shape, with the goal of generating circular footprints in the whole covered area. A HAPS scenario was selected here to test the procedure to synthesize the antenna beams, but the procedure is also applicable to any other lens antenna subsystem. The proposed method uses a full-wave time-domain software tool to optimize the lens. The usually prohibitive computer effort is greatly reduced here thanks to a set of design guidelines that suggest convenient initial values of the optimization parameters. As a proof of concept, a lens prototype is designed following the proposed procedure, built and measured.

The paper is organized as follows. After a presentation of the investigated scenario in Section 2, the method used to compute the footprints generated by the antenna beams is explained in Section 3. Section 4 shows the lens antenna concept used to fulfill the scenario requirements. The antenna design procedure is presented in Section 5 whereas the performances of the prototype are shown in Section 6. Finally, Section 7 concludes and summarizes the paper.

2. SCENARIO

In this section, a scenario suitable for HAPS communications is introduced. It consists of a multi-beam antenna that is supposed to be mounted on HAPS and provide 19 spot beams on the ground. This antenna is therefore well suited for Ka-band multi-cell architecture systems where each cell is served by a spot beam from the HAPS. The platform is intended to fly at the standard ground altitude of $H_{\text{HAPS}} = 21\,\text{km}$ [25] and the antenna payload is stabilized by a gimbal platform system that compensates for undesired movements of the station.

The cell boundary on the ground is determined by the $-4\,\text{dB}$ received power level with respect to the maximum power (P_{max}) received in the cell. The centers distance between adjacent cells should be then $d_{\text{cell}} = 4.33\,\text{km}$ to guarantee uniform power coverage of the illuminated area. Fig. 1 shows the arrangement and the used numbering scheme for the cells on the ground.

Figure 2 depicts the geometry considered here. The center of the antenna radiating element is the origin of the coordinate system. For each beam i, the boresight angle $\theta_{c,i}$, is then the angle formed by the center (CC_1) of the cluster, the antenna position and the center (CC_i) of the cell i.
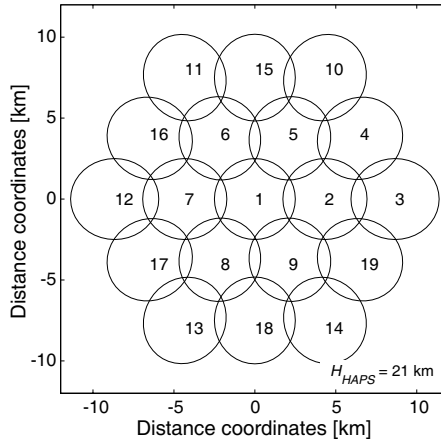
Figure 1. Enumeration and arrangement of the ground power footprints.

2.1. Scenario with 19 Identical Symmetric Beams

Beams with the same beam aperture generate a cluster with elliptical cell shapes. From geometrical considerations, the cell in the center of the cluster has a circular shape and its radius $R_{\text{cell},1}$ is associated to the $-4\,\text{dB}$ angle (FOV) of the beam simply by (1):

$$FOV = 2\arctan\left(\frac{R_{\text{cell},1}}{H_{\text{HAPS}}}\right) \tag{1}$$

Furthermore, the others cells ($i = 2, \ldots, 19$) of the cluster are elliptical (see Fig. 2), and they are characterized by a cell axial ratio (CAR) that depends from the boresight angle $\theta_{c,i}$ of each beam as (2):

$$CAR_i = \frac{H_{\text{HAPS}}\left[\tan\left(\theta_{c,i}+\frac{FOV}{2}\right)-\tan\left(\theta_{c,i}-\frac{FOV}{2}\right)\right]}{2H_{\text{HAPS}}\tan\left(\frac{FOV}{2}\right)\frac{1}{\cos\theta_{s,i}}}$$
$$\text{for } i = 2,\ldots,19 \tag{2}$$

In (2), the nominator is the longest semi-axis of the ellipse (CLA_i) whereas the denominator is the shortest one (CSA_i) and their expression can be deduced from Fig. 2 with simple trigonometric considerations.

In this scenario, beams characterized by a $FOV = 13.6°$ produce a cell in the center of the cluster with circular shape ($R_{\text{cell},1} = 2.5\,\text{km}$) and 18 asymmetric external cells. The cell centers and the associated boresight angles and cell axial ratios (CAR) are given in Table 1. CAR is frequently given as a percent deviation respect the perfect
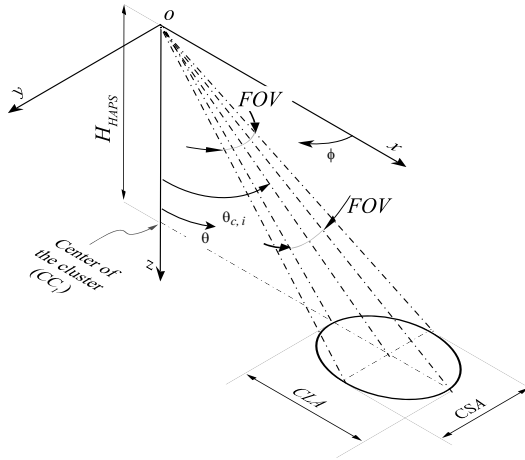
Figure 2. Down-link geometry using symmetric beams.

circular case. The cells surrounding the central cell #1 ($i = 2$, 5–9) are characterized by an axial ratio of 1.022 (i.e., 2.2% deviation respect to the circular case) while the most external cells ($i = 5$, 10–14) are characterized by an axial ratio of 1.084 (8.4%), and the remaining intermediate cells ($i = 4$, 15–19) are characterized by an axial ratio of 1.064 (6.4%).

2.2. Scenario with Asymmetrical Beams and Identical Cells

A cluster with all the cells identical and circular with radius R_{cell}, can be synthesized by using beams that are asymmetric with respect to their boresight axis. In such case, the beam aperture angle is not the same for all the beams of the cluster and three angles are needed to characterize the beams' shape. These angles are connected to three points $P_{A,i}$, $P_{B,i}$ and $P_{C,i}$ on the border of the i-th cell number as shown in Fig. 3. $P_{A,i}$ is the cell boundary point closest to the center of the cluster and $P_{C,i}$ is the opposite point to $P_{A,i}$ with respect to center CC_i of the cell. Point $P_{B,i}$ is easily obtained by considering the cell diameter perpendicular to $P_{A,i}$–$P_{C,i}$ (Fig. 3). Then, $\beta_{A,i}$, $\beta_{B,i}$ and $\beta_{C,i}$ are the angles between the center of the cell, the antenna and $P_{A,i}$, $P_{B,i}$ and $P_{C,i}$, respectively. The values of $\beta_{A,i}$, $\beta_{B,i}$ and $\beta_{C,i}$ can be deduced from Fig. 3 as follows:

$$\beta_{A,i} = \theta_{s,i} - \arctan\left(\frac{d_i - R_{\text{cell}}}{H_{\text{HAPS}}}\right) \quad \text{for } i = 2, \ldots, 19 \qquad (3)$$

Table 1. Data for the 19 considered cells in Fig. 1.

i	CC_i (x_i, y_i) [km]	d_i [km]	$\theta_{c,i}$ [deg]	CAR
1	(0, 0)	0	0	1
2	(4.330, 0)	4.330	11.65	1.022
3	(8.660, 0)	8.660	22.41	1.084
4	(6.495, 3.750)	7.500	19.65	1.064
5	(2.165, 3.750)	4.330	11.65	1.022
6	(−2.165, 3.750)	4.330	11.65	1.022
7	(−4.330, 0)	4.330	11.65	1.022
8	(−2.165, −3.750)	4.330	11.65	1.022
9	(2.165, −3.750)	4.330	11.65	1.022
10	(4.330, 7.500)	8.660	22.41	1.084
11	(−4.330, 7.500)	8.660	22.41	1.084
12	(−8.660, 0)	8.660	22.41	1.084
13	(−4.330, −7.500)	8.660	22.41	1.084
14	(4.330, −7.500)	8.660	22.41	1.084
15	(0, 7.500)	7.500	19.65	1.064
16	(−6.495, 3.750)	7.500	19.65	1.064
17	(−6.495, −3.750)	7.500	19.65	1.064
18	(0, −7.500)	7.500	19.65	1.064
19	(6.495, −3.750)	7.500	19.65	1.064

$$\beta_{B,i} = \arctan\left(\frac{R_{\text{cell}} \cos\theta_{c,i}}{H_{\text{HAPS}}}\right) \quad \text{for } i = 2, \ldots, 19 \tag{4}$$

$$\beta_{C,i} = \arctan\left(\frac{d_i + R_{\text{cell}}}{H_{\text{HAPS}}}\right) \quad \text{for } i = 2, \ldots, 19 \tag{5}$$

$$\beta_{A,i} = \beta_{B,i} = \beta_{C,i} = \arctan\left(\frac{R_{\text{cell}}}{H_{\text{HAPS}}}\right) \tag{6}$$

where d_i is the distance between the center of the cell i and the center of the cluster. In scenarios like the proposed one, in which the antenna is above the center of the cluster, the following relation is always valid: $\beta_{A,i} \leq \beta_{B,i} \leq \beta_{C,i}$. This motivates the necessity of asymmetric beams to achieve the desired cell shapes. These angles are used to set up initial constraints on the $-4\,\text{dB}$ beam aperture, in order to synthesize asymmetric beams generating circular cell footprints. More details are given in Section 5.
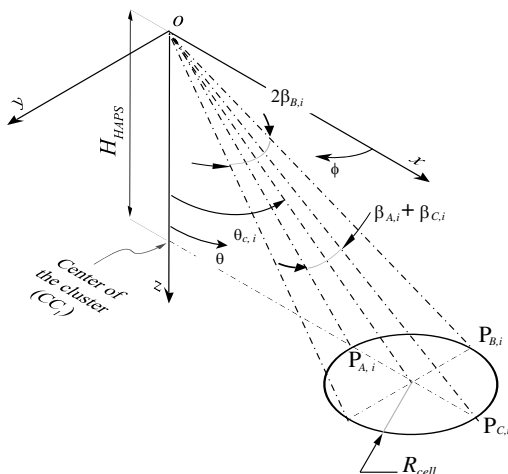
Figure 3. Down-link geometry using asymmetric beams to produce circular cells.

3. COMPUTATION OF GROUND POWER FOOTPRINTS AND OPTIMAL BEAM PATTERNS

The distribution of the power transmitted by each beam to its corresponding cell on ground can be computed using the Friis equation normalized to the transmitted power [26]. The free space path-loss between the antenna and the cell boundary has been taken into account in this work, since it affects strongly the cell shape.

The ground area covered by the footprints was discretized with a square grid of 10 m size. For each point on the grid $P(x, y)$, the power received from the i-th beam $P_{r,i}(x, y)$ was computed as:

$$P_{r,i}(x,y) = G_i(\theta, \phi) \left(\frac{\lambda}{4\pi \sqrt{x^2 + y^2 + H_{\text{HAPS}}^2}} \right)^2 \qquad (7)$$

where $G_i(\theta, \phi)$ is the radiation diagram of the i-th beam and λ the wavelength in free-space ($\lambda = 10.3\,\text{mm}$ at $f = 29\,\text{GHz}$) of the transmitted signal. The involved angles θ and ϕ are obtained from the points' coordinates $P(x, y)$ as follows:

$$\theta = \arctan \left(\frac{\sqrt{x^2 + y^2}}{H_{\text{HAPS}}} \right) \qquad (8)$$

$$\phi = \arg(x, y) \qquad (9)$$

In (7), both the radiation diagram of the beam and the free-space path loss contribute in determining the shape of the cell on the ground.

In general, the same amount of power is sought-after in each cell. Hence, when all the cells have the same circular shape, the desired optimal power distribution in each cell is just the ground power footprint generated by the beam 1 ($P_{r,1}(x, y)$), translated at the center of the other cells. Therefore, the optimal beam radiation pattern $G_i^{th}(\theta, \phi)$ that guarantees the desired footprint can be directly obtained from Eq. (7) as:

$$G_i^{th}(\theta, \phi) = \frac{P_{r,i}(x - x_i, y - y_i)}{\left(\frac{\lambda}{4\pi\sqrt{x^2+y^2+H_{\mathrm{HAPS}}^2}} \right)^2} \tag{10}$$

4. LENS ANTENNA CONCEPT FOR THE PROPOSED SCENARIOS

In this section, the antenna properties are determined according to the scenario specifications. The antenna system was realized by exciting a homogeneous Teflon lens with a set of circular waveguide feeds. This choice has been motivated in [27] and fully discussed in [28], where a design suitable for 7 cells cluster has been characterized. The extension of such an idea to a cluster with 19 cells is quite straightforward if every beam is produced independently by its corresponding feed. The 19 feed radiating apertures are placed in such a way that their radiation is focalized optimally by the lens (Fig. 4). Moreover, all the feeds' longitudinal axes intersect at the center of the lens and each feed points to the center of its cell. The feeds numbering scheme reproduces the one used for the cells.

## 4.1. Antenna System Based on Spherical Lens

A spherical lens focuses the radiation of the feeds, thus producing directive and symmetric beams [29, 30]. Provided that the distance of all the feed apertures from the lens surface is the same, the beams focalized by this lens exhibit the same radiation pattern. The theoretical directivity D_{th} of a circular radiating aperture that has a main beam with no sidelobes, is linked with the beam aperture Ω_{beam} (solid angle) and with the radius of the aperture R_{ap} by [27]:

$$R_{ap} = \frac{\lambda\sqrt{D_{th}}}{2\pi} = \frac{\lambda\sqrt{\frac{4\pi}{\Omega_{\mathrm{beam}}}}}{2\pi} \tag{11}$$
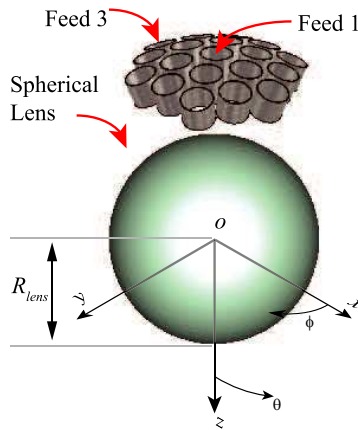
Figure 4. Model of the 3-D spherical dielectric lens antenna system. This antenna system generates 19 directive beams with symmetric main-lobe.
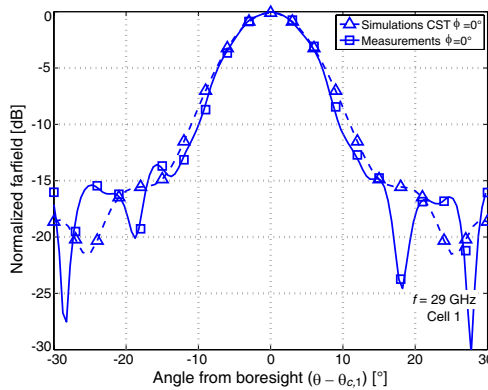
Figure 5. Farfield radiation pattern of the spherical lens. Comparisons between simulations and measurements.

Although a homogeneous Teflon lens exhibits always sidelobes [29–31] and their level depends essentially on the feeds' radiation and on the lens material, Eq. (11) can still be used to estimated correctly the aperture of a directive beam generated by a lens with radius, as demonstrated in [27]. Hence, Eq. (11) has been used here to figure out the lens dimensions for a needed beam aperture. The half power beam-width angle $\theta_{3\,dB}$ can be estimated by the $-4\,dB$ angle of the beam aperture (FOV) by using the usual cosine-square assumption

for the pattern [27], yielding:

$$\theta_{3\,\mathrm{dB}} = 0.88 FOV \tag{12}$$

so Eq. (11) can be transformed as:

$$R_{\mathrm{lens}} = \frac{\lambda\sqrt{\frac{4\pi}{\theta_{3\,\mathrm{dB}}^2}}}{2\pi} = \frac{\lambda\sqrt{\frac{4\pi}{(0.88 FOV)^2}}}{2\pi} \tag{13}$$

Note that (1) and (11) provide a model to link the geometry of the scenario (R_{cell}, H_{HAPS}) with the lens dimension (R_{lens}). Due to the lens symmetry and to the fact that in this design the adjacent waveguide feeds couple very weakly even in the close vicinity of the lens [27, 28], the 19 patterned beams generated by the lens antenna system modeled in Fig. 4 are identical and symmetric (see the simulated and measured radiation patterns in Fig. 5). These beam patterns have been used to compute the cells' power footprints according to Eq. (7). Figs. 6 and 7 show the power ground footprint of cells 1 and 3 predicted by using the simulated radiation pattern. Cell 1 is circular with a radius of 2.5 km, whereas cell 3 exhibits 8.8% of CAR. The same analysis has been performed for cell 2 and 4, yielding $CAR_2 = 2.8\%$ and $CAR_4 = 6.9\%$, in line with the values geometrical vales computed with (2). Figs. 8 and 9 depict the power footprints obtained by
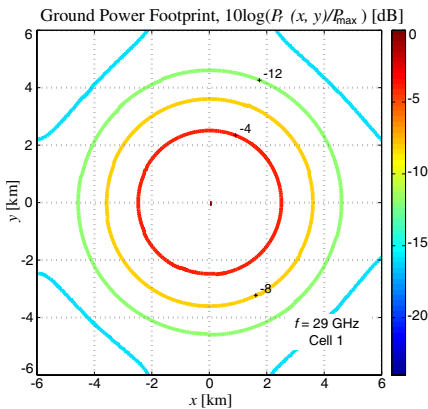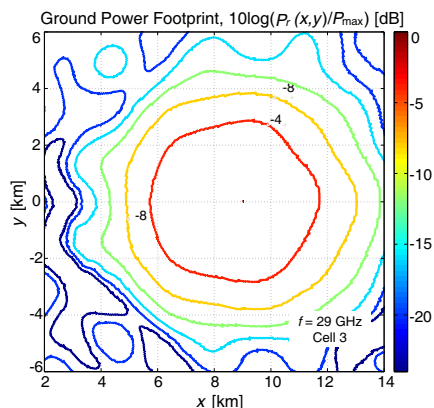

Figure 6. Footprint of cell 1 achieved with the spherical lens by using the simulated radiation pattern of beam 1. The cell boundary is a circle of 2.5 km radius.
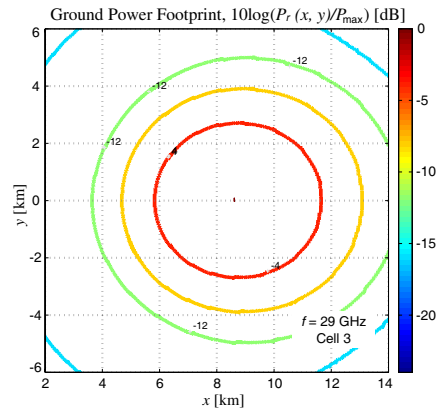
Figure 7. Footprint of cell 3 achieved with the spherical lens by using the simulated radiation pattern of beam 3. The cell boundary is an ellipse. The $-8\,\mathrm{dB}$ and the $-12\,\mathrm{dB}$ contour are elongated, as well.
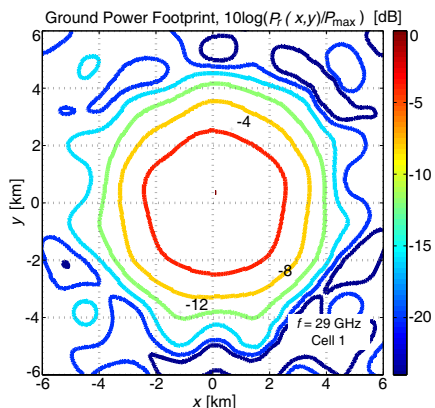
Figure 8. Footprint of cell 1 achieved with the spherical lens by using the measured radiation pattern of beam 1.

Figure 9. Footprint of cell 3 achieved with the spherical lens by using the measured radiation pattern of beam 3. The -4 dB, -8 dB and the -12 dB contours are elongated with respect to cell 1.

using actual measured radiation patterns. The agreement between the footprint values corresponding to simulated and measured radiation patterns is reasonably good in terms of shape, size and levels. The footprint of cell 3 is quite elongated along the x-axis, indicating a power spreading in this direction, as shown by the -4 dB, -8 dB and -12 dB contours.

4.2. Antenna System Based on Prolate Ellipsoidal Lens

In the previous section, we used the approximate analytical formulas (1) and (13) to design the spherical lens and to obtain the cells' dimensions. Here we consider an enhanced design in which the lens shape is slightly modified to take into account the beam asymmetry needed to satisfy the exact requirements in terms of beam aperture angles ($\beta_{A,i}$, $\beta_{B,i}$, $\beta_{C,i}$).

First, we note that the values of aperture angles $\beta_{A,i} + \beta_{C,i}$ and $2*\beta_{B,i}$ of Fig. 3 are very close to value of FOV of Fig. 2. Hence, we expect only minor modifications in the lens geometry with respect to the spherical case. Now, according to (13), a smaller beam aperture angle is achievable with a bigger lens dimension and vice versa. Since $\beta_{A,i} + \beta_{C,i}$ is smaller than $2*\beta_{B,i}$ for all the external cells of the cluster

and considering the rotational symmetry of the cluster with respect to the z-axis, we expect that the resulting lens shape is a prolate ellipsoid with two identical axes on the x-y plane and the longer axis on the z-axis (see Fig. 10). The equation of such ellipsoidal lens normalized to the shortest semi-axes is:

$$x^2 + y^2 + \frac{z^2}{LAR^2} = 1 \qquad (14)$$

where LAR is the lens axial ratio defined as the ratio between the longest (LLA) and the shortest (SLA) axis of the ellipsoid.

As it was done in the spherical lens case, an initial estimation of the lens dimensions (LLA and SLA) can be obtained using (13). But now, instead of FOV the beam aperture angles $\beta_{A,i} + \beta_{C,i}$ and $2*\beta_{B,i}$ are used to compute LLA and SLA respectively, yielding:

$$LLA_i = \frac{\lambda\sqrt{\frac{4\pi}{\left(0.88(2\beta_{A,i})\right)^2}}}{2\pi} + \frac{\lambda\sqrt{\frac{4\pi}{\left(0.88(2\beta_{C,i})\right)^2}}}{2\pi} \qquad (15)$$

$$SLA_i = \frac{\lambda\sqrt{\frac{4\pi}{\left(0.88(2\beta_{B,i})\right)^2}}}{\pi} \qquad (16)$$

The lens axial ratio (see Eq. (17)) is directly obtained dividing (15) by (16). The value of LAR of the cells situated at the same distance from
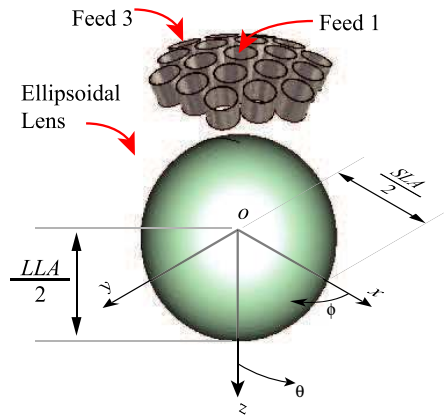

Figure 10. Model of the 3-D elipsoidal dielectric lens antenna system. This antenna system generates 19 directive beams with asymmetric main-lobe.

the center of the cluster is identical.

$$LLA_i = \frac{LLA_i}{SLA_i} = \frac{\frac{1}{\beta_{A,i}} + \frac{1}{\beta_{C,i}}}{\frac{1}{\beta_{B,i}}} \approx \frac{1}{\cos\theta_{c,i}} \quad \text{for } i = 2, \dots, 19 \qquad (17)$$

For practical reasons, only a value of LAR has to be chosen to perform the design of the lens so, following the procedure adopted in this paper, it is no possible to fully compensate the ellipticity of all the cells of the cluster at the same time (see next Section 5). The system specifications associated to this research called for an optimization of the lens shape providing circular shapes in the most external cells of the cluster (cell 3, 10–14), where the ellipticity produced by using a spherical lens would have been more evident. The lens symmetry guarantees the circularity of cell 1 whereas SLA fixes its dimension. By ensuring the circularity of the shape of cell 1 and of the external cells of the cluster, we logically also expect a reduction of the ellipticity of the remaining cells (cell 4, 15–19, 2, 5–9) with respect to the spherical lens case. However, the shape of these intermediate cells can not be fully controlled by the simple lens design procedure proposed here.

A final consideration concerns the solution of Eqs. (2) and (17). The cell axial ratio and the lens axial ratio have been computed for different θ_c within the angle range $0° \leq \theta_c \leq 50°$. Fig. 11 graphically proves that the function $1/\cos\theta_c$ is the solution of Eq. (17) and for $\theta_c \leq 30°$ it can be considered a good approximation of Eq. (2). This comparison highlights the fact that to compensate the axial ratio of a cell produced by a symmetric beam pointing in the θ_c direction, an ellipsoidal lens with $LAR = 1/\cos\theta_c$ is a good initial candidate. Thus, we can use the relation $CAR_i = LAR_i = 1/\cos\theta_c$ to initiate a design of an ellipsoidal lens for the scenario depicted in Fig. 3. The full ellipsoidal lens design procedure is given in the next section.
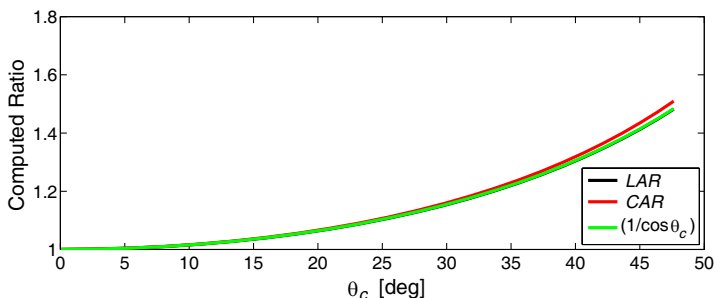
Figure 11. Computed lens axial ratio and cell axial ratio for different value of θ_c. The two curves are compared with $1/\cos\theta_c$.

5. ELLIPSOIDAL LENS DESIGN PROCEDURE

The complete ellipsoidal lens design procedure is based on full-wave optimization. The analyzed geometry is depicted in Fig. 10. Because of the symmetry of the cluster, we optimize the lens activating only feeds 1 and 3 in the analysis. This simplifies the design process and allows, at the same time, the possibility of optimizing both the dimensions and the shape of the cells of the cluster.

Before starting the optimization process, the optimal radiation pattern $G_1^{th}(\theta, \phi)$ and $G_3^{th}(\theta, \phi)$ are computed with (10). Indeed these optimal patterns guarantee the desired circular contour for cells 1 and 3, compensating adequately the effect of the free-space path-loss.

The two parameters of the lens to be optimized are SLA and LAR. Eqs. (16) and (17) give the initial value of SLA and LAR, respectively. In our case $SLA = SLA_1 = 60$ cm and, since we are interested in minimize axial ratio of the most external cells, $LAR = LAR_3 = 1/\cos\theta_{c,3} = 1.082$.

For every combination of the two parameters, the radiation patterns of beams 1 and 3 was computed by full-wave analysis (CST Microwave Studio $^{©}$ [32]) and compared with the sought-after optimal patterns. The optimization cost function was set up classically in terms of some threshold values $(\delta_1, \delta_2, \dots)$ for the differences between the computed and optimal radiation pattern. In this process, the use of the pre-computed optimal patterns $(G_1^{th}(\theta, \phi)$ and $G_3^{th}(\theta, \phi))$ avoids the calculation of the ground power footprint at the end of each iteration, thus accelerating the optimization.

In order to speed up the optimization procedure and to maintain at the same time a reliable output, the radiation patterns are evaluated only in some reference angle values (see Eqs. (18)–(21)). Such values correspond to the most relevant directions of the cells boundary (i.e., the directions singled out by the segments, $\overline{OA}$, $\overline{OB}$ and $\overline{OC}$ in Fig. 3).

$$\left| G_1(\theta, \phi)|_{\theta=FOV/2, \phi=0} - G_1^{th}(\theta, \phi)\Big|_{\theta=FOV/2, \phi=0} \right| \leq \delta_1 \qquad (18)$$

and similarly, for the beam 3:

$$\left| G_3(\theta - \theta_{c,3}, \phi)|_{\theta=\beta_{C,3}, \phi=0} - G_3^{th}(\theta - \theta_{c,3}, \phi)\Big|_{\theta=\beta_{C,3}, \phi=0} \right| \leq \delta_2 \qquad (19)$$

$$\left| G_3(\theta - \theta_{c,3}, \phi)|_{\theta=\beta_{B,3}, \phi=90} - G_3^{th}(\theta - \theta_{c,3}, \phi)\Big|_{\theta=\beta_{B,3}, \phi=90} \right| \leq \delta_3 \qquad (20)$$

$$\left| G_3(\theta - \theta_{c,3}, \phi)|_{\theta=\beta_{A,3}, \phi=180} - G_3^{th}(\theta - \theta_{c,3}, \phi)\Big|_{\theta=\beta_{A,3}, \phi=180} \right| \leq \delta_4 \quad (21)$$

The constraint on the boresight direction of each beam has been relaxed because preliminary full-wave simulations demonstrated that for the cases considered here, the steering of the beam due to the ellipsoidal lens can be neglected (less than 0.1 degrees).

A last word must be said about the lens focal distance. which obviously changes with any modification of the lens geometry. Therefore, the feeds have to be moved to the new focal points to maximize the radiation performances and reduce the side-lobe levels. At a first glance, this appears as a drawback in this method since it would slow down the whole optimization process. But, thanks to the accurate initial values used in the optimization process, only a few iterations are necessary to find the optimal geometry.

## 6. CHARACTERIZATION OF THE ELLIPSOIDAL LENS PROTOTYPE

The optimal patterns $G_1^{th}(\theta, \phi)$ and $G_3^{th}(\theta, \phi)$ for the critical beams #1 and #3 have been computed using Eq. (10). They are shown in Fig. 12 and 13, respectively. The radiation pattern of beam #1 is symmetric with respect to its boresight direction. The half-power beamwidth of this beam is 11.9°, the beamwidth at $-4\,$dB is 13.5° and the sidelobe level is lower than $-15\,$dB, as expected from [27]. The radiation pattern of beam #3 is asymmetric, being more directive in the $\phi = 0°$ plane than in the $\phi = 90°$ plane, as expected by the relation $\beta_{A,i} + \beta_{C,i} < 2 * \beta_{B,i}$ discussed in Section 4.2. Furthermore, in the $\phi = 0°$ plane, beam #3 presents an asymmetry between its right $(\theta - \theta_{C.3} > 0°)$ and left $(\theta - \theta_{C.3} < 0°)$ sides. This is also expected by the fact that in Fig. 3 the circular shape of the cell 3 is guaranteed by $\beta_{C,i} < \beta_{A,i}$.

An ellipsoidal lens has been designed following the designed procedure proposed in Section 5. The optimal values of LAR and SLA achieved at the end of the optimization are 1.08 and 57.8 mm, respectively. The radiation patterns of the beams 1 and 3 achieved by full-wave simulation and the optimal patterns $G_1^{th}(\theta, \phi)$ and $G_3^{th}(\theta, \phi)$ are in very good agreement (Figs. 12 and 13) confirming that our optimization process yields a lens design that satisfies our optimization goal. It is interesting to note that the initial values of SLA and LAR computed before the optimization process by Eqs. (16) and (17) are very close to the optimized ones, demonstrating the robustness of our design approach. Furthermore, only three iterations have been performed to conclude the optimization procedure.

The ellipsoidal lens prototype has been realized by milling machine techniques with a nominal tolerance of 50 μm to guarantee the best
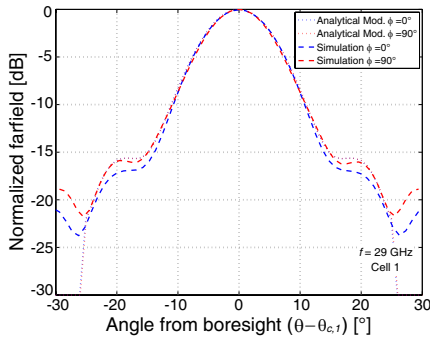
Figure 12. Farfield radiation pattern of beam #1. Comparison between optimal and simulated patterns for cuts $\phi = 0°$ and $\phi = 90°$. The symmetry of beam #1 is readily apparent.
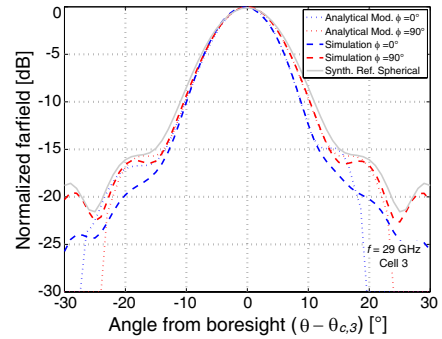
Figure 13. Farfield radiation pattern of beam #3. Comparison between optimal and simulated patterns for cuts $\phi = 0°$ and $\phi = 90°$. Beam #3 is asymmetric and more directive than beam #1. Beam #3 is asymmetric and more directive than beam #1.
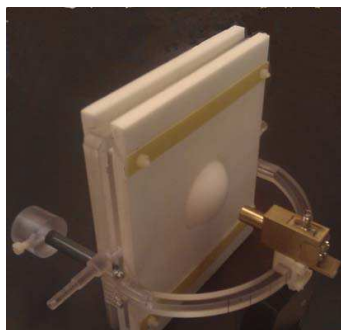

Figure 14. Ellipsoidal lens prototype under machining. (a) The lens alignment during the machining process is guarantee by metal clumps. (b) The CNC machine manufactures the lens surface.

shape accuracy. Fig. 14 shows the lens prototype during the machining process. Metal clumps have been machined to accurately align the lens during its realization. A digital micrometer has been used to verify the quality and dimensions of the final machined prototype which is shown in Fig. 15.

Figure 15. Ellipsoidal lens prototype.

Figure 16. Ellipsoidal lens prototype with a waveguide feed.

6.1. 2D Radiation Pattern Measurements

The performance of the lens has been characterized through measurements of the radiation pattern in anechoic chamber. In addition to the lens, the antenna subsystem includes a linearly polarized primary source maintained in place by a plastic frame [27], which also allows a fine control of the relative position between the waveguide feed and the lens. The test set-up is shown in Fig. 16.

The optimal patterns $G_1^{th}(\theta, \phi)$ and $G_3^{th}(\theta, \phi)$ have been compared with the measurement data for the two main cut planes $\phi = 0°$ and $\phi = 90°$. The farfield patterns of the ellipsoidal lens antenna (only one feed is active at one time) are plotted in Figs. 17 and 18. The agreement between theory and measurements is good, especially within the angle range $|\theta - \theta_{c,i}| \leq 10°$ where the pattern is determinant for the right cell shape.

6.2. Ground Power Footprint Generated by the Simulated and Measured Data
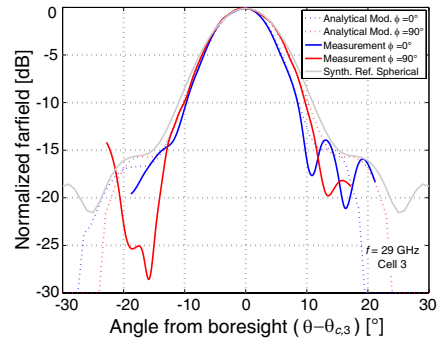
Simulated and measured radiation patterns of the ellipsoidal lens have been used to compute the ground power footprints.

Figures 19 and 20 show the footprint of cell 1 achieved with, respectively, the simulated and measured radiation pattern. Good agreement between simulations and measurements can be observed. The contour at -4 dB (that delimits the cell boundary) is circular and its diameter is 4.95 km, approaching closely the scenario requirements.

Figures 21 and 22 show the footprint of cell 3 achieved with the simulated and measured radiation pattern respectively. A good agreement between simulations and measurements can be observed
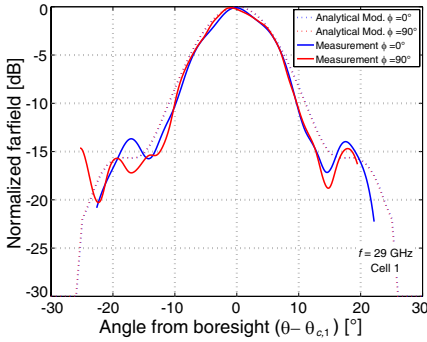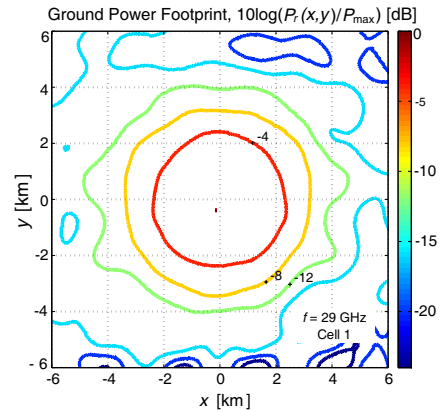
Figure 17. Farfield radiation pattern of beam 1. Comparison between optimal and measured patterns. Good agreement is observed.
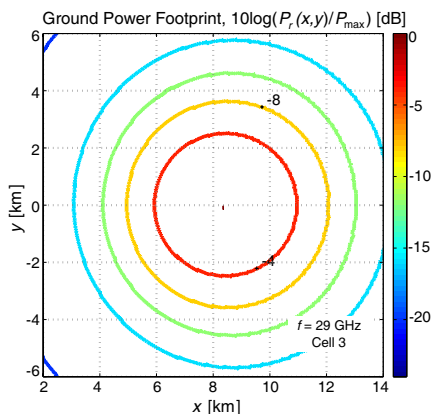

Figure 18. Farfield radiation pattern of beam 3. Comparison between optimal and measured patterns. Good agreement is observed. Beam 3 is asymmetric and more directive than beam 1.
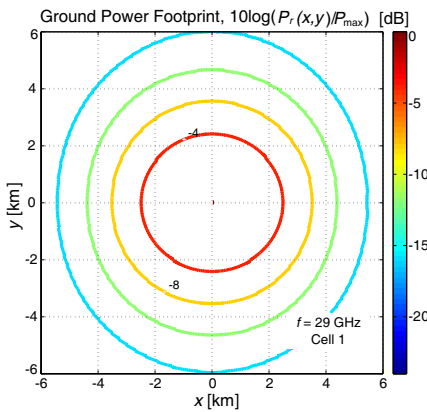
Figure 19. Footprint of cell 1 achieved with the ellipsoidal lens by using the simulated radiation pattern of beam 1. The cell boundary is a circle with 2.475 km radius.

Figure 20. Footprint of cell 1 achieved with the ellipsoidal lens by using the measured radiation pattern of beam 1.
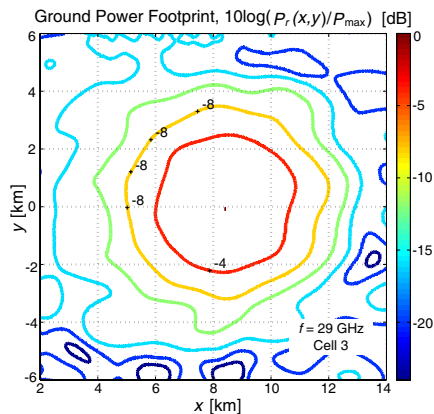
Figure 21. Footprint of cell 3 achieved with the ellipsoidal lens by using the simulated radiation pattern of beam 3. The cell boundary is a circle with 2.505 km radius.

Figure 22. Footprint of cell 3 achieved with the ellipsoidal lens by using the measured radiation pattern of beam 3.

also in this case. The footprint contour at -4 dB is again circular and its diameter is 5.01 km. Fig. 21 clearly shows that the elliptical cell shape produced by a symmetric beam (as shown in Fig. 7) is fully compensated with the designed lens. Furthermore, the cell is centered in the position expected by Table 1 confirming that in this scenario the ellipsoidal lens has a negligible influence in steering the beam radiated by the primary source.

Figures 19–22 show also globally that out of the -12 dB contour the footprint quality degrades in general. This is probably due to the presence of sidelobes, but is a slightly concern here since the region where the shape should be controlled is within the cell boundary.

For the sake of completeness, the shape of the footprints has been also characterized for intermediate cells 2 and 4 (not directly controlled by the optimization process) in order to investigate the validity of the proposed strategy. Table 2 summarizes the results for the relevant cells #1 to #4. All the cells have now practically circular foot prints and even in the worst-case cells #2 and #4 the improvement of the axial ratio is evident.

6.3. Application to More Demanding Scenarios

As evidenced in Table 1 the scenario that originally motivated this paper implies footprints that deviate only slightly from a circular shape

Table 2. Properties of the most relevant cells.

i	CAR Spherical	CAR Ellipsoidal	CLA, CSA Spherical [km]	$(P_{C,i}$–$P_{A,i})$, $2(P_{B,i}$–$CC_i)$ Ellipsoidal [km]
1	1	1	5, 5	4.95, 4.95
2	1.022	0.985	5.11, 5.22	4.93, 5
3	1.084	1	5.42, 5.88	5.01, 5.01
4	1.064	0.990	5.32, 5.66	4.95, 5
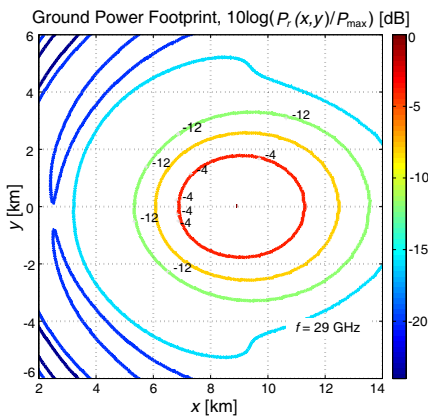
Figure 23. Original footprint for the very high elevation angle considered in the scenario of Section 4.1 spherical lens produced a very elongated −4 dB footprint with an ellipticity of 1.230.
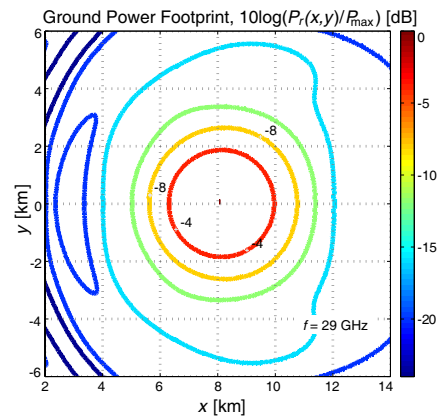
Figure 24. Improved footprint for the very high elevation angle considered in the scenario of Section 4. The new prolate ellipsoidal lens produces an almost circular −4 dB footprint with an ellipticity of 1.005.

(max axial ratio to be corrected 8.4%) and are therefore not very challenging. In this section, we show the capabilities of the prolate ellipsoidal lens design procedure developed in this paper to deal with much more elongated cells. To this purpose, we select a scenario in which the antenna operates at 12 km altitude (instead of 21 km) and the most critical cells are characterized by a higher elevation angle $\theta_c = 33.7°$. This corresponds to cells which are 8 km offset from the center of the cluster. Fig. 23 shows the ground footprint achieved

when a spherical Teflon lens of 60 mm of diameter is used. The cell boundary is characterized by an ellipticity of 23%. According to the procedure presented in Section 5, a prolate ellipsoidal lens with $LAR = 1/\cos\theta_c = 1.120$ should correct this cell ellipticity by generating asymmetric beams. Fig. 24 shows the cell shape achieved with such a modified lens. Despite the high elevation angle, the cell shape is now practically circular with a percent CAR lower than 0.5%. In this particularly extreme situation, a slight beam steering, apparent in Fig. 24, is introduced by the elliptical lens. However this small value (around 1 degree) can be easily compensated by a mechanical repositioning of the corresponding feed.

7. CONCLUSION

The capabilities of a Ka-band prolate ellipsoidal shaped dielectric lens antenna for generating asymmetric beams producing circular ground footprints have been investigated. Our analysis revealed that the problem of elongated footprints generated by spherical lenses located in traditional aerial platforms can be solved via the optimization of the lens shape. The new ellipsoidal shape is obtained with a set of simple analytical design equations, eventually enhanced by full-wave optimizations. A properly designed prolate ellipsoidal lens can simultaneously and efficiently focus beams radiated by several independent waveguide feeds adequately placed around its surface. The comparison between the ellipsoidal lens and the spherical lens (both optimized to operate properly in the same scenario) has shown that ellipsoidal lens improves the circularity of all the beam footprints generated by the antenna, which is of particular interest in airborne-based communication systems.

The proposed lens design procedure can be applied to both small and quite large values of the footprint cell elongation. Moreover, the use of prolate ellipsoid lenses do not increase neither the technological complexity nor the required computational resources during the antenna design process.

Minor collateral effects of the ellipsoidal lens are a small beam steering (but only at very high elevation angles), easily compensated by adjusting the feed angle, a slight change in focal distances and the deformation of the footprints for lower power levels outside the -4 dB boundary. This last effect is probably due to the lens sidelobes. It could be eventually reduced by using a stratified lens and by adding a matching layer, which would also increase the lens efficiency. These questions are out of the scope of this paper but should be the of further research.

ACKNOWLEDGMENT

REFERENCES

1. Carrasco, E., M. Arrebola, J. A. Encinar, and M. Barba, "Demonstration of a shaped beam reflectarray using aperture-coupled delay lines for LMDS central station antenna," *IEEE Trans. Antennas Propagat.*, Vol. 56, 3103–3111, Oct. 2008.

2. Charvat, G. L., L. C. Kempel, E. J. Rothwell, C. M. Coleman, and E. L. Mokole, "An ultrawideband (UWB) switched-antenna-array radar imaging system," *IEEE Int. Symp. on Phased Array Systems and Technology*, 543–550, Oct. 2010.

3. Rao, S., M. Tang, C.-C. Hsu, and J. Wang, "Advanced antenna technologies for satellite communication payloads," *1st European Conference on Antennas and Propagation, Proc. EuCAP*, 2006.

4. Averty, F., A. Louzir, J. F. Pintos, P. Chambelin, C. Person, G. Landrac, and J. P. Coupez, "Cost effective antenna for LEO-satellites communication system using a homogeneous lens," *IEEE Antennas and Propagation Society International Symp.,* Vol. 1, 671–674, Jun. 2004.

5. Xu, Z., G. White, and Y. Zakharov, "Optimisation of beam pattern of high-altitude platform antenna using conventional beamforming," *Proc. IEE*, Vol. 153, No. 6, 865–870, Dec. 2006.

6. Fonseca, N. J. G. and J. Sombrin, "Multi-beam reflector antenna system combining beam hopping and size reduction of effectively used spots," *IEEE Trans. Antennas Propagat.*, Vol. 54, 88–99, Apr. 2012.

7. Costa, J. R., E. B. Lima, and C. A. Fernandes, "Compact beam-steerable lens antenna for 60-GHz wireless communications," *IEEE Trans. Antennas Propagat.,* Vol. 57, 2926–2933, Oct. 2009.

8. Chreim, H., R. Chantalat, M. Thèvenot, U. Naeem, S. Bila, T. Monédière, B. Palacin, Y. Cailloce, G. Caille, and P. De Maagt, "An enhanced Ka-band reflector focal-plane array using a multifeed EBG structure," *IEEE Antennas and Wireless Propagat. Lett.,* Vol. 9, 1152–1156, 2010.

9. Thornton, J., "A low sidelobe asymmetric beam antenna for

high altitude platform communications," *IEEE Microw. Wireless Comp. Lett.,* Vol. 14, No. 2, 59–61, Feb. 2004.

10. Katzis, K. and D. Grace, "Inter-high-altitude-platform handoff for communications systems with directional antennas," *Radio Science Bulletin,* No. 330, 29–38, Mar. 2010.

11. Palma-Lazgare, I. R. and J. A. Delgado-Penin, "WiMAX HAPS-based downlink performances employing geometrical and statistical propagation-channel characteristics," *Radio Science Bulletin,* No. 330, 50–66, Mar. 2010.

12. Abella, C., J. Peces, M. Marín, J. Martinez, and K. Markus, "Development of a compact antenna for global earth coverage," *Proc. 23rd Eur. Microwave Conf.,* 906–908, Madrid, Spain, Oct. 1993.

13. Lin, S.-M., Y.-Q. Wang, and P.-L. Shen, "Phase-only synthesis of the shaped beam patterns for the satellite planar array antenna," *Proc. IEEE*, 331–334, 2000.

14. Martínez-Lorenzo, J., "A shaped and reconfigurable reflector antenna with sectorial beams for LMDS base station," *IEEE Trans. Antennas Propagat.,* Vol. 54, No. 4, Apr. 2006.

15. Koleck, T., "Active antenna coverage synthesis for GEO satellite using genetic algorithm," *Proc. Int. Symp. on Antennas and Propagat.,* 142–144, 2003.

16. Villegas, F. J., "Parallel genetic-algorithm optimization of shaped beam coverage areas using planar 2-D phased arrays," *IEEE Trans. Antennas Propagat.,* Vol. 58, 604–608, Feb. 2010.

17. Córcoles, J., J. Rubio, and M. Á. González, "Spherical-wave-based shaped-beam field synthesis for planar arrays including the mutual coupling effects," *IEEE Trans. Antennas Propagat.,* Vol. 59, 2872–2881, Aug. 2011.

18. Liu, Y., Q. H. Liu, and Z. Nie, "Reducing the number of elements in the synthesis of shaped-beam patterns by the forward-backward matrix pencil method," *IEEE Trans. Antennas Propagat.,* Vol. 55, 1745–1753, Jun. 2007.

19. Smulders, P. F. M., "Exploiting the 60 GHz band for local wireless multimedia access: Prospects and future directions," *IEEE Commun. Mag.,* Vol. 40, No. 1, 140–147, Jan. 2002.

20. Costa, J. R., C. A. Fernandes, G. Godi, R. Sauleau, L. Le Coq, and H. Legay, "Compact Ka-band lens antennas for LEO satellites," *IEEE Trans. Antennas Propagat.,* Vol. 56, 1251–1258, May 2008.

21. Letizia, M., J.-F. Zürcher, B. Fuchs, C. Z. Gastón, and J. R. Mosig, "Circularly polarized multi-beam lens antenna

system. Comparison between 2 polarizers," *6th European Conference on Antennas and Propagation, Proc. EuCAP*, 2012.

22. Sauleau, R. and B. Barès, "A complete procedure for the design and optimization of arbitrarily-shaped integrated lens antennas," *IEEE Trans. Antennas Propagat.,* Vol. 54, No. 4, 1122–1133, Apr. 2006.

23. Rolland, A., R. Sauleau, and L. Le Coq, "Flat-shaped dielectric lens antenna for 60-GHz applications," *IEEE Trans. Antennas Propagat.,* Vol. 59, No. 11, 4041–4048, Nov. 2011.

24. Letizia, M., B. Fuchs, C. Zorraquino, J. F. Zürcher, and J. R. Mosig, "Oblique incidence design of meander-line polarizers for dielectric lens antennas," *Progress In Electromangeics Research*, Vol. 45, 309–335, 2012.

25. Aragon-Zavala, A., J. L. Cuevas-Ruiz, and J. A. Delgado-Penin, *High-Altitude Platforms for Wireless Communications*, 5–15, John Wiley and Sons, 2008.

26. Haykin, S., *Communication Systems*, 4th Edition, 518–522, John Wiley and Sons, 2001.

27. Letizia, M., B. Fuchs, A. Skrivervik, and J. R. Mosig, "Circularly polarized lens antenna system providing multibeam radiation pattern for HAPS," *Radio Science Bulletin*, No. 330, 18–28, Mar. 2010.

28. Letizia, M., J.-F. Zürcher, B. Fuchs, J. R. Mosig, and A. Skrivervik, "Circularly polarized lens antenna system for high altitude platforms (HAPS)," *5th European Conference on Antennas and Propagation, Proc. EuCAP*, 2011.

29. Balanis, C. A., *Antenna Theory*, 2nd Edition, 45–86, John Wiley and Sons, New York, 1997.

30. Balanis, C. A., *Antenna Theory*, 2nd Edition, 575–560, John Wiley and Sons, New York, 1997.

31. Sanford, J., "Scattering by spherically stratified microwave lens antennas," *IEEE Trans. Antennas Propagat.*, Vol. 42, No. 5, 690–698, May 1994.

32. www.cst.com